

## Growth of ZnO Submicron Single-Crystalline Platelets, Wires, and Rods by Ultrasonic Spray Pyrolysis

Myo Than HTAY\*, Yoshio HASHIMOTO, and Kentaro ITO

Department of Electrical and Electronic Engineering, Faculty of Engineering, Shinshu University, 4-17-1 Wakasato, Nagano 380-8553, Japan

(Received June 5, 2006; revised August 31, 2006; accepted October 22, 2006; published online January 10, 2007)

Submicron single crystals of ZnO were grown by spray pyrolysis: the mist of an aqueous solution was generated by ultrasonic agitation and then pyrolyzed on a heated glass substrate. Hexagonal platelets of ZnO 10–90 nm thick were obtained when ammonium acetate was incorporated into the precursor solution of zinc acetate. Single-crystalline wires and rods, which were 50–150 and 300–4000 nm thick respectively, were obtained when indium nitrate was co-incorporated into the solution as a metal catalyst. The crystallographic direction of wires and rods was parallel to one of the [0001], [10 $\bar{1}$ 0], or [11 $\bar{2}$ 0] axis of wurtzite. As substrate temperature increased, the aspect ratio of the crystal thus tended to decrease. Structural and compositional analyses of these crystals were performed by scanning electron microscopy, scanning ion microscopy, transmission electron microscopy and electron diffraction, X-ray diffraction, X-ray photoelectron spectroscopy, and energy dispersive X-ray spectroscopy. [DOI: 10.1143/JJAP.46.440]

KEYWORDS: ZnO, platelets, wires, rods, ultrasonic spray pyrolysis, seeding layer, seed crystallites, growth mechanism

### 1. Introduction

ZnO, a II–VI compound wide-bandgap (3.37 eV at room temperature)<sup>1)</sup> oxide semiconductor, is well known as a multi-functional material for its versatile properties such as wide-ranging conductivity, high voltage–current nonlinearity, high optical transmittance, UV emission,<sup>2)</sup> piezoelectricity,<sup>3,4)</sup> sensitivity to gases<sup>5)</sup> and chemical agents, and catalytic activity<sup>6)</sup> in either intrinsic or extrinsic nature. It has good potential in many applications such as transparent conductive electrodes, sensors, semiconductor optoelectronic devices, optical circuits, nanodevices, surface coating films and so on.

Up to now, single crystals as well as polycrystals of ZnO with wurtzite structure can be grown in the form of bulk or thin film by means of various physical and chemical preparation techniques. Besides these structures, ZnO is also known to be able to grow into various submicron crystal forms such as whiskers,<sup>7,8)</sup> nanobelts,<sup>9)</sup> nanorods,<sup>10)</sup> nanowires,<sup>11)</sup> nanopowders,<sup>12)</sup> and so on. These submicron structures of ZnO are expected to have special functions in accordance with their particular physical geometry such as crystal size, crystalline density, structural orientation and aspect ratio. Law *et al.* suggested that the application of crystalline ZnO nanowires array as an anode in dye-sensitized solar cell<sup>13)</sup> improves the rapid collection of carriers generated throughout the device. Lee *et al.* reported that a well-aligned ZnO nanowires show sufficient brightness as a field emitter, which is promising for the application of a glass-sealed flat panel display of the near future.<sup>14)</sup> Various growth techniques such as high-temperature vacuum deposition techniques,<sup>11,15–19)</sup> hydrothermal solution synthesis,<sup>20)</sup> solution-based method,<sup>21)</sup> electrochemical deposition in porous membranes,<sup>22–24)</sup> and frame spray pyrolysis method<sup>25)</sup> were used for fabrication of these submicron structures. However, there are still problems in direct fabrication of large arrays of complex submicron structures with controlled crystalline morphology, orientation and surface architectures for practical applications.

In this paper we will report on controlled synthesis of ZnO

submicron crystalline platelets, wires and rods by a simple, cost-effective and efficient method of ultrasonic spray pyrolysis. In this method, a liquid solvent containing an appropriate precursor is atomized by ultrasonic vibration, and then the generated mist is transported by a carrier gas to a heated substrate where pyrolysis or decomposition process takes place. This method was adopted for preparing transparent conductive ZnO films<sup>2)</sup> and sintered powders<sup>26)</sup> for decades. To the best knowledge of the authors, however, the growth of the submicron ZnO structures by spray pyrolysis was not reported previously.

### 2. Experimental Procedure

Preparation of ZnO submicron crystals was carried out by using a home-made ultrasonic spray pyrolysis system. The schematic diagram of the system was shown in Fig. 1. It was mainly composed of three sections called an atomization unit, a transportation system, and a decomposition zone.

In the atomization unit, five pieces of 2.4 MHz piezoelectric vibrators (Honda Electronics, HM-2412) were used as an ultrasonic source. For atomization, the vibration was applied indirectly via transmission medium liquid (water only) and 0.05 mm thick polytetrafluoroethylene (Teflon) sheet to the liquid precursor solution, which was put inside the atomization chamber jacketed with a cooling water system. Temperature of the chamber was detected by means of a thermometer.

In the transportation system, pure nitrogen gas (99.9999%) controlled by a mass flow meter (KOFLOC, RK-1150) was used for conveying precursor mist that was generated in the atomization chamber and then carried to the decomposition zone: it passed through a primary transport tube, liquid trap, secondary transport tube, and finally through a vertically opened quartz nozzle. By passing through the liquid trap, re-condensed mist or large-grain mist could be filtered so that only vapor including fine-grain mist was transported to the substrate where product was collected. The vertically opened quartz nozzle composed of 2 mm orifices shown in the left hand side of Fig. 2 was designed in order to obtain uniform fine products.

In the decomposition zone, a vertical infrared-gold-image lamp (ULVAC, E-25) was used as a heater so that precise

\*E-mail address: s06t215@shinshu-u.ac.jp

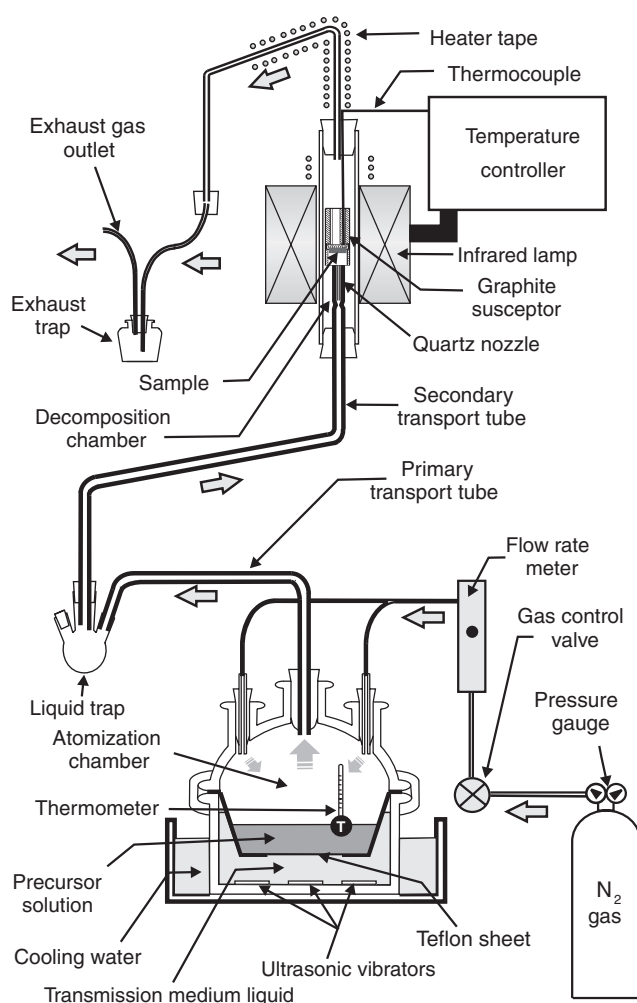


Fig. 1. Schematic diagram of ultrasonic spray pyrolysis system.

temperature control was achieved. A soda-lime glass substrate (SLG,  $L15 \times W10 \times T1.5 \text{ mm}^3$  in size) on which crystal growth took place was heated indirectly by means of a specially designed graphite susceptor shown in the right hand side of Fig. 2. By using this heating technique, it is possible to avoid overheating of incoming precursor mist before it reaches the desired location for decomposition. A distance between the substrate and nozzle tip was set at 8 mm. Vertical upward feeding of mist to the substrate has the advantage of obtaining fine products because large-grain mist that tends to degrade products quality is more unlikely to reach the substrate against gravitational force than the highly mobile fine-grain mist, the average size of which may be of the order of one micrometer according to eq. (2.1) proposed by Lang,

$$d = \kappa \left( \frac{8\pi\sigma}{\rho f^2} \right)^{1/3}, \quad (2.1)$$

where  $d$  is the diameter of mist,  $\kappa$  is the system constant,  $\sigma$  is the surface tension, and  $\rho$  is the density of the solution, and  $f$  is the frequency of the vibration source (2.4 MHz).<sup>27)</sup> The exhaust vapor was sent out to the atmosphere after passing through an exhaust trap where neutralization process takes place.

For sample preparation, source solutes for a precursor solution were chosen in order to satisfy essential conditions

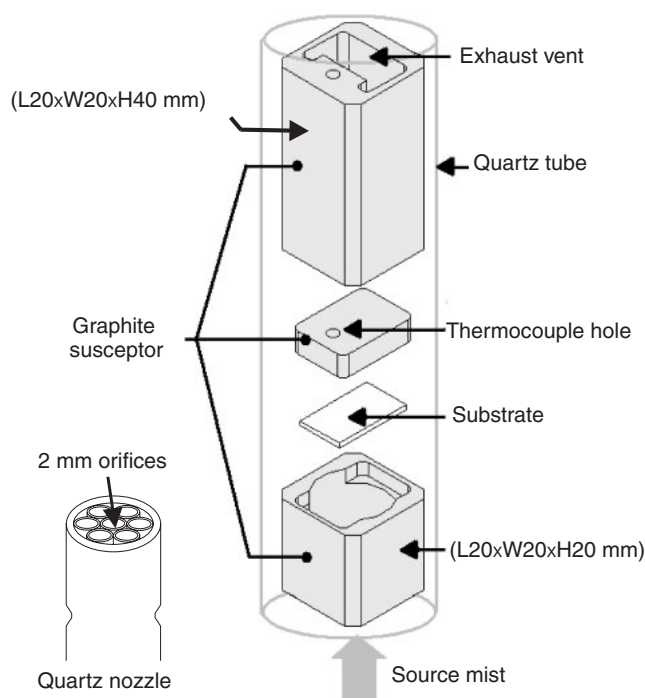


Fig. 2. Structure of quartz nozzle (left) and graphite susceptor (right).

such as stability at room temperature, non-oxidizing in air or in the presence of water vapor, and having low decomposition temperatures preferably higher than its boiling or sublimation temperature. With these criterions, zinc acetate dihydrate (abbreviated to ZA, Wako, 99%) was used as a source species for Zn, and only de-ionized water which also acts as solvent for the precursor solution was used as an O source. Indium(III) nitrate trihydrate (abbreviated to IN, Wako, 98%) was used as a source species for In which may act as metal catalyst for growing rod-shaped crystals. Ammonium acetate (abbreviated to AA, Wako, 97%) was added to adjust the pH of solution. An ISFET pH meter (Shindengen, KS701) was used to measure solution's pH. Two types of samples were prepared to investigate the effect of precursor solution on growth nature. Type I was prepared by incorporating AA (5 times mole ratio of N to Zn) into the ZA precursor solution and type II was prepared by incorporating both AA (5 times mole ratio of N to Zn) and IN (one tenth mole ratio of In to Zn). The initial concentration of ZA in each precursor solution was set at 0.3 mol/L. Flow rate of carrier gas ( $\text{N}_2$ ) was set at 1.4 L/min during growth process. The influence of growth temperature on crystal morphology was studied at 300, 400, and 500 °C for both types.

Crystal surface morphology was studied using a field emission scanning electron microscope (FE-SEM; Hitachi, S-4100) and scanning ion microscope (SIM; Seiko, SMI-2050,  $\text{Ga}^+$  ion). Crystalline structures of the samples were analyzed by using X-ray diffraction (XRD; Rigaku, RINT-2200V/PCSV,  $\text{Cu } K\alpha$  ray;  $\lambda = 1.5405 \text{ \AA}$ ). Transmission electron microscopy (TEM; JEOL, JEM-2010,  $\text{LaB}_6$  cathode) analysis was carried out at an acceleration voltage of 200 kV. An X-ray photoelectron spectroscope (XPS; Surface Science Instruments, S-probe 7339,  $\text{Al } K\alpha$  1486.6 eV source) and an energy dispersive X-ray spectroscope

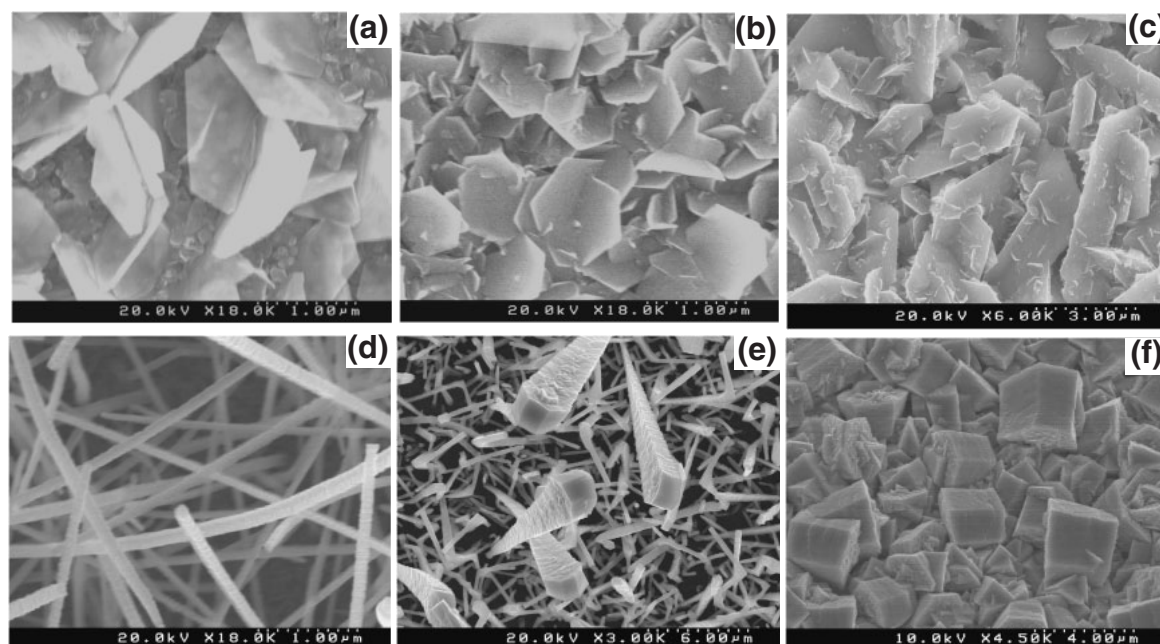


Fig. 3. SEM images showing surface morphology of type I samples grown for 120 min at (a) 300, (b) 400, (c) 500 °C, and type II samples grown for 120 min at (d) 300, (e) 400, (f) 500 °C.

(EDX; JEOL, 7000F/IV) was used to estimate the composition of samples.

### 3. Results and Discussion

Figures 3(a) to 3(c) show the SEM images of type I samples grown for 120 min at different growth temperatures. It is clearly observed that hexagonal-shaped crystalline platelets are grown. At 300 °C, partially extruded hexagonal platelets with a width ranging from 1.5 to 2.0  $\mu\text{m}$  and a thickness of 10–30 nm are grown at a density of about 1.5 billion platelets per square centimeter. At 400 °C, mutually interlaced hexagonal platelets of 400 to 600 nm in width and of 30–50 nm in thickness are obtained and the growth density is about 10 billion platelets per square centimeter. At a higher temperature of 500 °C, densely interlaced hexagonal platelets with a width varied between 1.5–5.0  $\mu\text{m}$ , a thickness ranged from 40 to 90 nm and with a growth density of about 6 billion platelets per square centimeter are obtained. Due to the interlaced structures, these platelets seem to be bonded firmly to each other. This kind of surface nature may be useful for applications such as gas sensors,<sup>28)</sup> an *eta*-solar cell<sup>29,30)</sup> and dye-sensitized solar cells,<sup>13,31,32)</sup> in which a large surface area is necessary. From the results discussed above, we may say that growth temperature seems to have a great influence on the size, orientation and growth density of the platelets.

Surface morphologies of type II samples grown at different temperatures are shown in Figs. 3(d) to 3(f). At the growth temperature of 300 °C, as can be seen in Fig. 3(d), crystalline wires with a thickness of 50–150 nm and a length up to about 10  $\mu\text{m}$  are obtained. Here we use the term “crystalline wires” for those with a thickness less than 200 nm and the term “crystalline rods” for larger ones. At 400 °C, the crystallization takes place more rapidly and results in the growth of larger crystalline rods having a thickness of 0.3–0.6  $\mu\text{m}$  and a length up to 10  $\mu\text{m}$ . Together

with these rods, extra large crystalline rods with a thickness of 2–4  $\mu\text{m}$  and a length of about 10–30  $\mu\text{m}$  are also found to co-exist [see Fig. 3(e)]. From the appearances of these wires and rods as shown in Fig. 4, we may expect their crystallographic direction to be along one of the [0001], [10 $\bar{1}$ 0], or [11 $\bar{2}$ 0] axis of wurtzite. In the case of samples prepared at 500 °C, growth of polyhedrons with a width of 2–4  $\mu\text{m}$  and a height of 1–3  $\mu\text{m}$  are observed [see Fig. 3(f)]. It seems that at the high growth temperature, an isotropic crystallization is accelerated and thus made dominant over the unidirectional crystal growth so that only polyhedron structures are formed rather than the rod-shaped ones. As the growth temperature increases, the structure changes from wires, followed by rods, to polyhedrons. In the other words, the aspect ratio (ratio of height to width) of submicron crystalline structure decreases with increasing growth temperature.

The crystal structure of all these samples is identified as wurtzite by XRD patterns shown in Fig. 5. By comparing the patterns shown in this figure, it is to be noticed that the peak intensity of each crystal face is different at different growth temperatures. In type I sample prepared at 300 °C, peaks due to the (10 $\bar{1}$ 0), (10 $\bar{1}$ 1), and (11 $\bar{2}$ 0) faces are strong while (0002), (10 $\bar{1}$ 2), and (10 $\bar{1}$ 3) faces are very weak [see Fig. 5(b)]. If samples are prepared at higher growth temperatures, however, the former peaks become weaker, while the latter peaks become stronger [see Figs. 5(c) and 5(d)]. This tendency may be directly related to the change in aspect ratio and orientation of these hexagonal crystalline structures for each growth temperature. The opposite tendency is the case in type II samples. A strong (0002) peak is dominating at 300 °C [see Fig. 5(e)], while (10 $\bar{1}$ 0) and (10 $\bar{1}$ 1) peaks are found to be dominant in the sample prepared at 400 and 500 °C [see Figs. 5(f) and 5(g)].

The bright-field TEM image of a crystalline wire grown at 300 °C is shown in Fig. 6(a). The corresponding selected

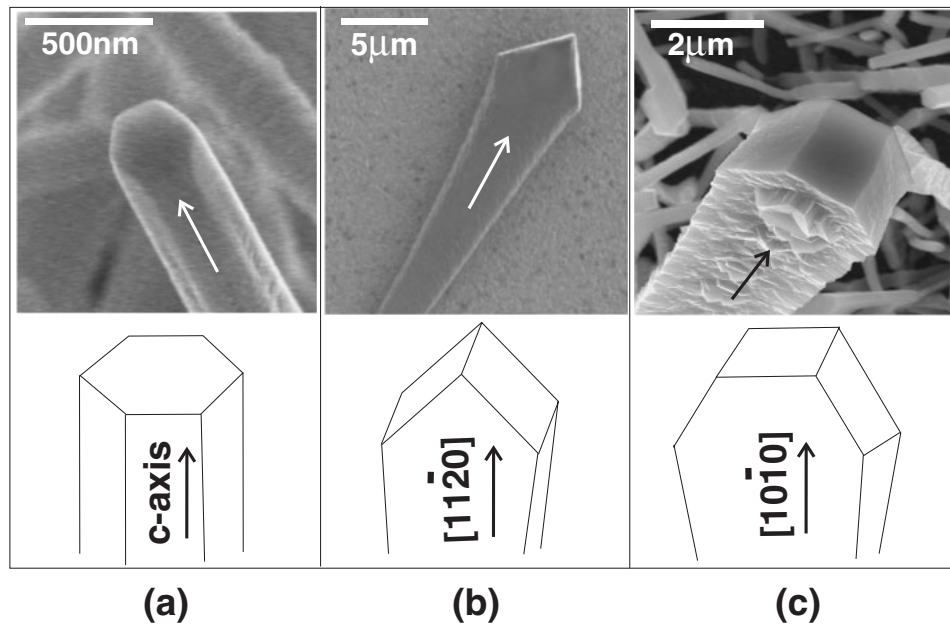


Fig. 4. SEM images showing morphology of the crystalline rods grown along (a)  $[0001]$  or  $c$ -axis, (b)  $[11\bar{2}0]$  axis, (c)  $[10\bar{1}0]$  axis. The bottom pictures illustrate the respective crystallographic direction of wurtzite.

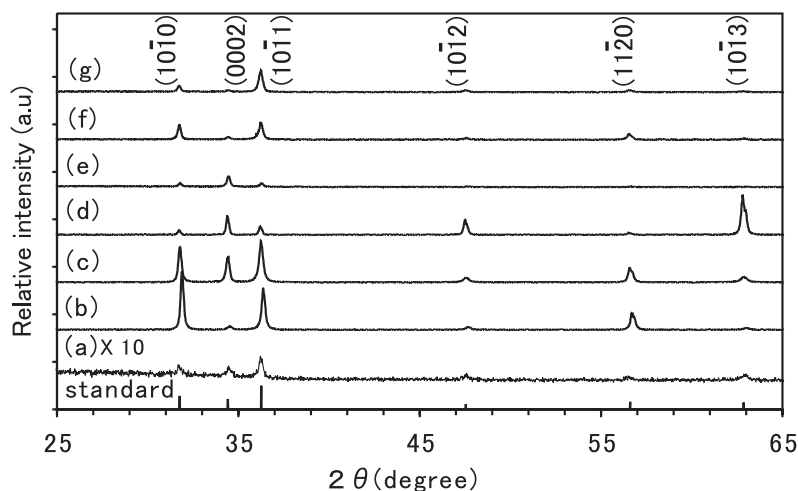


Fig. 5. XRD patterns of type I samples prepared at (b) 300, (c) 400, (d) 500 °C, and type II samples prepared at (e) 300, (f) 400, and (g) 500 °C. The pattern (a) is taken from the SL grown for 30 min. The intensity of (a) is multiplied by 10 for visual enhancement. The bottom pattern is a standard powder pattern for wurtzite ZnO.

area electron diffraction pattern (SAED) and high-magnification TEM image are shown in Figs. 6(b) and 6(c), respectively. According to the SAED pattern, the wire is grown along the  $[0001]$  or  $c$ -axis. This agrees with the fact that the wire has the shape of a hexagonal prism as shown in Fig. 4(a). The lattice spacing of  $(0001)$ ,  $(0002)$ , and  $(10\bar{1}0)$  planes are equal to 5.36, 2.68, and 2.87 Å, respectively, which is consistent with the XRD measurement and the theoretical values. The high-magnification TEM image exhibits lattice fringes perpendicular to the growth direction and has the spacing of about 2.60 Å which is in good agreement with the spacing of the  $(0002)$  plane estimated from the SAED pattern. The bright-field TEM image and its corresponding SAED pattern of the crystalline rods grown at 400 °C are shown in Figs. 6(d) and 6(e), respectively. From the bright-field TEM image, we can see that the tip of the thick crystalline rod is triangular while those of the thin crystalline rods are relatively flat [see the right side of the thick rod shown in Fig. 6(d)]. The SAED pattern for the

encircled area exhibits hexagonally symmetric spots. This indicates the existence of single crystalline rod grown along the  $[11\bar{2}0]$  direction as shown in Fig. 4(b). The lattice spacing of a  $(11\bar{2}0)$  plane is equal to 1.69 Å. This value is close to half of a theoretical value of  $a = 3.24982$  Å, which is the lattice spacing of  $(1000)$  plane for wurtzite. The  $(10\bar{1}0)$  plane, which makes an angle of 30° with the  $(11\bar{2}0)$  plane, has the lattice spacing of 2.87 Å. This result is also consistent with the SAED pattern taken from the  $[\bar{1}2\bar{1}0]$  direction.

Figure 7(a) shows the EDX spectrum which is measured at the tip of the single-crystalline wire grown along the  $c$ -axis. The corresponding SEM image is shown in the inset. The strong (weak) peaks appear due to Zn and O (Si and In). The Si peak is assigned to arise from the SLG substrate using a compositional mapping (not shown here). It is thus supposed that the tip is mainly composed of ZnO containing less than 1 at. % of In. Similar result was obtained from the EDX spectrum taken from the tip of the rod grown along the



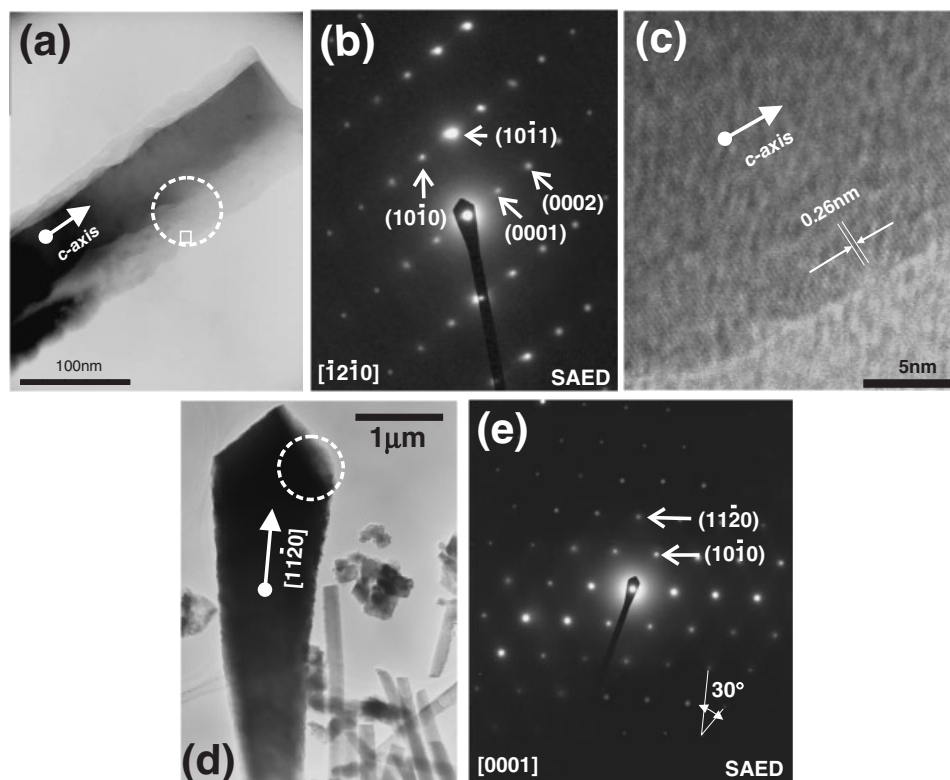


Fig. 6. TEM images and SAED patterns of ZnO crystalline wire and rod. (a) Bright field image of ZnO wire prepared at 300 °C. (b) SAED pattern of the encircled area shown in (a). (c) High-magnification image of the squared area in (a), showing lattice fringes of (0002). (d) Bright field image of ZnO rods prepared at 400 °C. (e) SAED pattern of the encircled area shown in (d).

$[10\bar{1}0]$  axis as shown in the inset of Fig. 7(b). According to the compositional mapping, the compositions of the bumpy structure and its nearby region of the tip are identified to be the same with each other. This means that the bumpy structure and the tip itself are ZnO. The growth of whiskers has often been explained by a vapor–liquid–solid (VLS) growth mechanism<sup>33,34</sup> where their tips consist of an alloy with a low melting point. However, the EDX results show that the tips of the present ZnO wires and rods do not contain enough amounts of In to reduce the melting point of the alloy. We did not observe any clue for the existence of metal alloy particles in these crystalline structures during TEM analysis either. In the conventional VLS method, catalytic metals are pre-deposited before the growth of wires or rods. In the present ultrasonic spray pyrolysis, however, catalytic metal source as well as Zn and O sources are delivered onto the substrate simultaneously. In this case, therefore, we consider that a stable oxide of the catalytic metal could be easily formed rather than a low melting point metal alloy.

In order to understand the growth mechanism for these submicron crystalline structures, the growth morphology was investigated by SEM micrography of the samples prepared under different growth periods (30, 60, and 120 min). Figures 8(a) and 8(b) show the surface morphologies of type II samples grown at 300 °C for 30 and 60 min, respectively. From Fig. 8(a), which represents the early stage of growth process, we can confirm clearly that the formation of thin layer takes place dominantly on the substrate rather than the growth of crystalline wires. We later call this thin layer as a seeding layer (SL). After SL with the thickness less than 100 nm covers the whole surface of the

substrate, the clusterization of tiny crystal seeds from the SL into a seed crystallite (SC) may take place and then the unidirectional nucleation and growth seem to prevail on it, thus resulting in the growth of crystalline wires as shown in Fig. 8(b). Here, we refer “SC” for “the starting crystal seed” that was formed probably by the clusterization of tiny crystal seeds right after the formation of SL during the early stage of growth. We presume that the SC’s may contribute as the origin of growth for the crystalline wires and rods, i.e., the SC’s may behave as the favorite sites for the crystal growth. In Fig. 8(c), an SIM image of the sample prepared for 120 min at 300 °C is shown. A dark square region in this figure represents the place where the SL is completely etched off by focused ion beam (FIB) process. The arrow in this figure points the place, where a crystalline wire is grown locally on the SL. Figure 8(d) shows the surface morphologies of type II samples grown at 400 °C for 30 min. It is also found that the growth at a higher temperature is similar to that mentioned above, however it takes place with a much higher growth rate so that larger SC’s are obtained on the SL which can be seen as protruded bright objects in the figure. In Fig. 8(e), the surface morphology of the sample grown at 400 °C for 60 min is shown. Short crystalline rods whose tips still maintain the form of the previous SC’s can be observed in this figure. When the growth period is increased to 120 min, these rods are found to be grown into longer rods as shown in Fig. 8(f). From these examinations, we may say that the density, length and size of wires and rods have increased with the growth period and temperature. In addition to this, we can presume that the SC’s embedded in the SL give rise to the needle-like crystals whose growth

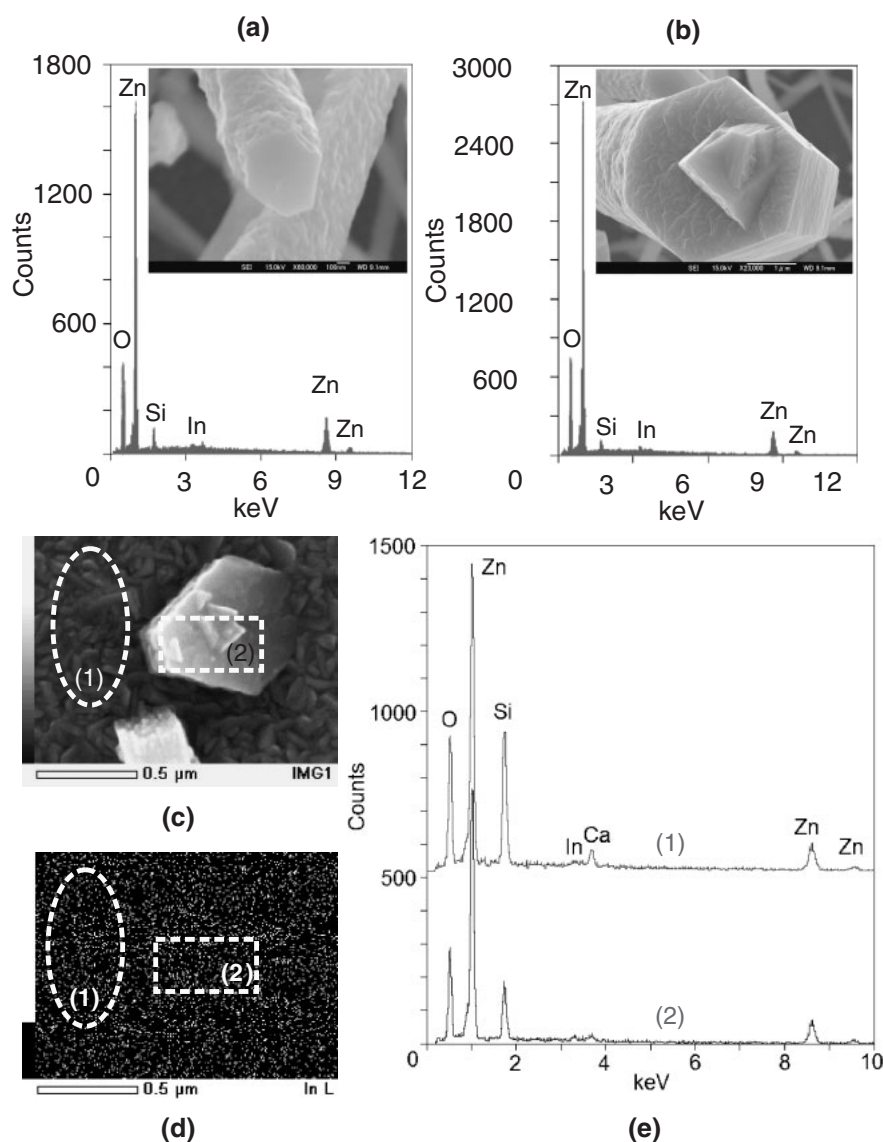


Fig. 7. EDX spectra taken from the tip of the submicron crystalline rod grown along (a)  $c$ -axis and (b)  $[10\bar{1}0]$  axis. The inset shows the corresponding SEM image of the region from which the spectrum was taken. (c) SEM image showing SL and SC: region (1) represents the SL and (2) for the SC. (d) Compositional mapping result showing the distribution of In for the region shown in (c). (e) EDX spectra for the selected regions in (c): spectrum (1) represents for the region (1) and (2) for the region (2) of (c).

orientation and aspect ratio are dependent on the orientations of SC and the preparation conditions such as growth temperature.

In order to understand the properties of SL and SC's, the XRD measurement as well as XPS and compositional mapping by EDX were carried out on the sample prepared for 30 min which has the surface morphology of the initial growth stage as shown in Fig. 9(a). In this high magnification SEM image, we can clearly see the partially protruded hexagonal crystal islands on the relatively flat SL. From hexagonal appearance of these islands, we can speculate these islands to be the ZnO crystal seeds which we refer as the SC's. Only wurtzite phase of ZnO is identified by the XRD measurement as can be seen in Fig. 5(a). From this result, we can confirm that the SL and SC's are composed of randomly orientated ZnO crystals. In XPS measurement, the incorporation of In up to 1 at.% is detected. The chemical shift of In 3d spectrum to a higher binding energy side (+1.5 eV) from the standard metal In 3d spectrum is

observed. There exists an indium oxide compound such as  $\text{In}_2\text{O}_3$  in the SL in accordance with our speculation discussed above. However, due to a very small amount of  $\text{In}_2\text{O}_3$  in the SL, we could not identify the existence of an  $\text{In}_2\text{O}_3$  phase from the XRD pattern. The depth profile of In 3d spectrum is shown in Fig. 9(b). Here, pattern (a) represents the top surface of SL, and (c) the bottom of SL. There is no obvious difference in the chemical shift between the surface and the bottom. This may explain that the  $\text{In}_2\text{O}_3$  phase has been formed since the initial stage of the SL growth. Because the  $\text{In}_2\text{O}_3$  has a very high melting point ( $1913^\circ\text{C}$ ), it is hardly conceivable that it is in a liquid state at growth temperatures ( $300$  and  $400^\circ\text{C}$ ) of the present method. Incidentally, the conventional VLS method which involves the metallic catalyst consisting of Au needs much higher temperatures (above  $800^\circ\text{C}$ ).<sup>11,19</sup> Figure 7(d) shows the compositional mapping of In distribution for the region shown in Fig. 7(c). The region (1) represents the thin SL and the region (2) the protruded SC in the figure. We can see

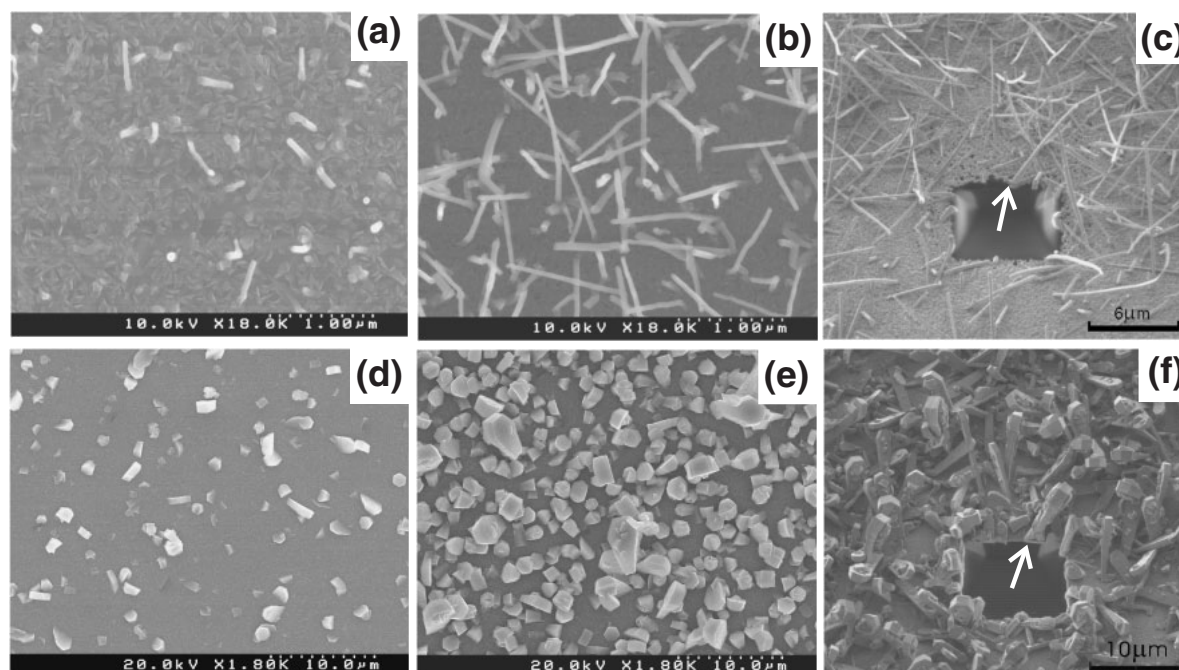


Fig. 8. SEM images of samples prepared for (a) 30 min at 300 °C, (b) 60 min at 300 °C, (d) 30 min at 400 °C, (e) 60 min at 400 °C. SIM images (bird's eye view) showing etched area of the SL by FIB for the sample grown at (c) 300 °C for 120 min, (f) 400 °C for 120 min. The arrows indicate the places where a crystalline wire or rod is grown locally on the SL.

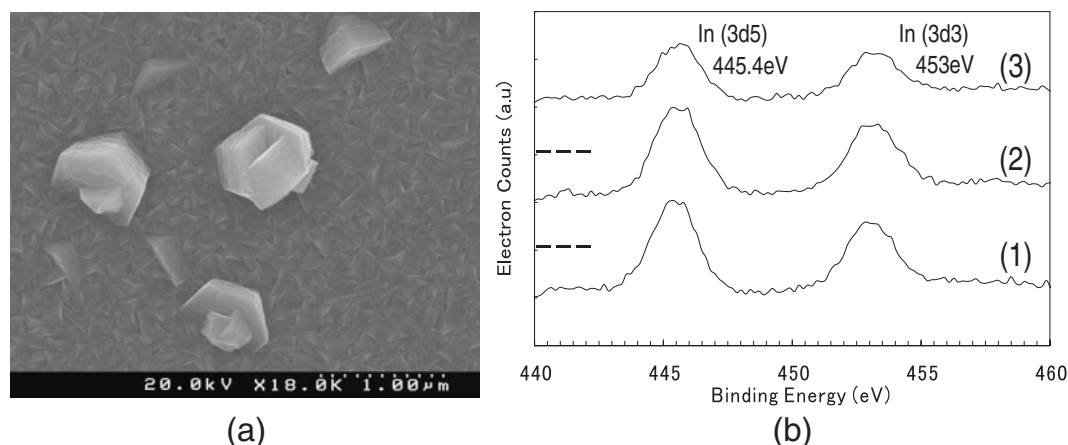


Fig. 9. (a) High magnification SEM image showing the hexagonal SC's on SL. (b) XPS spectrum of In 3d taken at (1) the top surface, (2) the depth etched for 5 min by Ar ion sputtering, and (3) the bottom (etched for 35 min) of SL.

that there is no obvious difference in the distribution of In between the SL and SC. By comparing the two corresponding EDX spectra for the highlighted regions as shown in Fig. 7(e), we can see the stronger intensities of Si and Ca in region (1) since these Si and Ca peaks are originated from the SLG substrate. Furthermore, there are no obvious changes in the relative intensity of Zn, O, and In between the two regions. Therefore, we may conclude that the chemical composition between the SL and SC are quite similar.

Based on the analysis discussed above, we propose a possible growth mechanism for these submicron crystalline structures of ZnO as depicted in Fig. 10. Initially, precursor mist may evaporate and decompose to form the vapor that is composed of an active source species as it approaches to the heated substrate. An SL is then deposited from the vapor by

a CVD-like mechanism as Viguié and Spitz explained for spray pyrolysis.<sup>35)</sup> It is followed by the clusterization of tiny crystal seeds into the SC's on the SL layer. Finally, the growth of SC's into various submicron crystalline structures may take place depending on the growth conditions. However, more works are still necessary to fully explain this growth mechanism.

The additives in the precursor solution may have an influence on seeding nature. In the case of AA incorporation (type I sample), almost uniform growth rate in the  $\langle 10\bar{1}0 \rangle$  and  $\langle 11\bar{2}0 \rangle$  directions is enhanced resulting in  $\langle 0002 \rangle$  hexagonal-faced platelets [see Figs. 3(a) to 3(c)]. Without incorporation of AA, only polycrystalline thin films consisting of irregular-shaped grains was obtained as reported in conventional spray pyrolysis.<sup>2,36-44)</sup> In type II samples which are prepared under IN co-incorporation, unidirectional

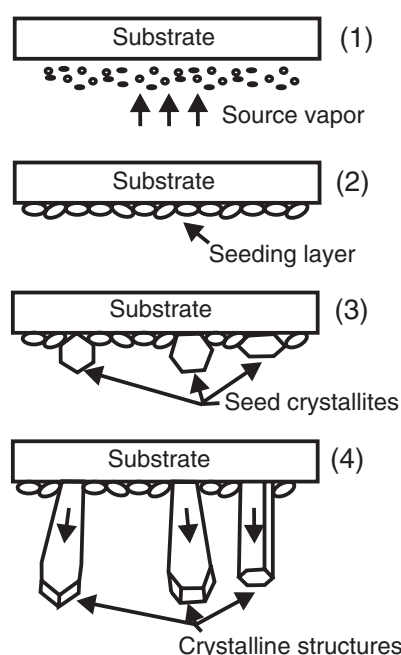


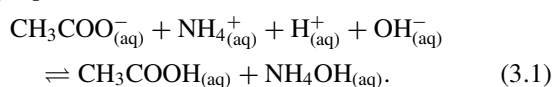
Fig. 10. Possible growth mechanism: step (1) evaporation and decomposition of vapor, (2) formation of SL, (3) formation of SC's, and (4) growth of crystalline structures.

Table I. pH of various precursor solutions.

No.	ZA : IN : AA mole ratio	pH
1	1 : 0 : 0	6.6
2	0.3 : 0 : 0	6.8
3	1 : 0 : 1.5	7.2
4	0.3 : 0 : 1.5	7.2
5	1 : 0.03 : 1.5	7.2
6	0.3 : 0.03 : 1.5	7.2
7	0.3 : 0.01 : 1.5	7.2

growth along one of the  $c$ -axis,  $[10\bar{1}0]$  or  $[11\bar{2}0]$  axis is enhanced, resulting in one-dimensional crystalline structures as represented in Fig. 4.

Table I shows the pH values of the precursor solution under different concentrations of ZA and IN. The result indicates that by the addition of AA, the pH value of the precursor solution is stabilized at 7.2 at room temperature independent of the concentrations of ZA and IN. This may be due to the contribution of AA (hydrolysis into  $\text{NH}_4\text{OH}$  and  $\text{CH}_3\text{COOH}$ ) in the solution as a buffer agent that resists a change in pH even though the concentration of the ZA and IN varies. According to Le Chatelier's principle, this stabilization phenomenon can be explained by the shift of reversible chemical equilibrium of AA solution shown in the following eq. (3.1).



If there is an increase of acidic species in the precursor solution, the reaction that yields more alkaline species like hydroxide compounds may take place. In the case of excess alkaline species, the reaction which produces acidic species such as ethanoic acid may be dominant. As a result, no net

change in the pH of the solution occurs. Stabilizing the solution's pH during atomization may have the effect to enhance the feeding of homogeneous source vapor to the substrate and thus realizes the uniform decomposition and the growth in the preferred directions of crystal seeds, resulting in hexagonal platelets, wires, rods, and polyhedrons of wurtzite ZnO on a wide area of the glass substrate in a reproducible manner.

#### 4. Conclusions

By feeding the mist of an aqueous precursor solution upward in ultrasonic spray pyrolysis, it was possible to supply source vapor onto a glass substrate homogeneously. By using a graphite susceptor, the unnecessary infrared heating of the incoming source vapor was avoided so that decomposition process was easy to control.

Submicron platelets of wurtzite ZnO were obtained with an ammonium acetate buffer agent incorporated in the zinc acetate precursor solution. At a growth temperature of 300 °C, hexagonal platelets 10–30 nm thick and 1.5–2.0 μm wide were obtained with a density of about 1.5 billion platelets per square centimeter. At 400 °C (500 °C), mutually interlaced hexagonal platelets 30–50 nm (40–90 nm) thick and 400–600 nm (1.5–5.0 μm) wide were observed with a density of about 10 (6) billion platelets per square centimeter.

Using the precursor solution in which indium(III) nitrate was co-incorporated as an In metal catalyst, we obtained crystalline wires 50–150 nm thick and up to about 10 μm long and rods 0.3–4.0 μm thick and up to 30 μm long. The higher the substrate temperature, the larger was the thickness of wires and rods, the length of which was parallel to one of the  $[0001]$ ,  $[10\bar{1}0]$ , or  $[11\bar{2}0]$  axis of wurtzite. However, the ZnO crystal grown on the substrate at 500 °C was an aggregate of polyhedral grains a few microns in size.

As a whole, we may conclude that the nature of precursor solution and the substrate temperature have a great influence over the crystalline morphology such as orientation, and aspect ratio of the submicron crystals.

#### Acknowledgment

One of the authors (M. T. Htay) would like to express gratitude to the Ministry of Education, Culture, Sports, Science and Technology of Japan for grant of postgraduate scholarship. Special thanks are due to Mr. Isamu Minemura for many help with construction of experimental apparatus and Mr. Tomohiko Yamakami for TEM photography.

- 1) Y. F. Chen, D. M. Bagnall, H. Koh, K. Park, K. Hiraga, Z. Zhu, and T. Yao: *J. Appl. Phys.* **84** (1998) 3912.
- 2) M. H. Choi and T. Y. Ma: *J. Mater. Sci.* **41** (2006) 431.
- 3) J. Molarius, J. Kaitila, T. Pensala, and M. Ylilammi: *J. Mater. Sci.* **14** (2003) 431.
- 4) Z. L. Wang and J. Song: *Science* **312** (2006) 242.
- 5) J. Xu, Y. Chen, and J. Shen: *J. Nanosci. Nanotechnol.* **6** (2006) 248.
- 6) Y. Q. Huang, M. D. Liu, Y. K. Zeng, and S. B. Liu: *J. Inorg. Mater.* **16** (2001) 391.
- 7) C. X. Xu, X. W. Sun, B. J. Chen, Z. L. Dong, M. B. Yu, X. H. Zhang, and S. J. Chua: *Nanotechnology* **16** (2005) 70.
- 8) T. Yasui, M. Yasuda, D. Nezaki, M. Takata, B. P. Zhang, and Y. Segawa: *Thin Solid Films* **464–465** (2004) 273.
- 9) X. D. Bai, P. X. Gao, and Z. L. Wang: *Appl. Phys. Lett.* **82** (2003) 4806.



- 10) C. X. Xu, A. Wei, X. W. Sun, and Z. L. Dong: *J. Phys. D* **39** (2006) 1690.
- 11) Y. Wu, H. Yan, M. Huang, B. Messer, J. H. Song, and P. Yang: *Chem.—Eur. J.* **8** (2002) 1260.
- 12) S. Park, J. C. Lee, and D. W. Lee: *J. Mater. Sci.* **38** (2003) 4493.
- 13) M. Law, L. E. Greene, J. C. Johnson, R. Saykally, and P. Yang: *Nat. Mater.* **4** (2005) 455.
- 14) C. J. Lee, T. J. Lee, S. C. Lyu, Y. Zhang, H. Ruh, and H. J. Lee: *Appl. Phys. Lett.* **81** (2002) 3648.
- 15) U. Krishnamachari, M. Brogstrom, B. J. Ohlsson, N. Panev, L. Samuelson, W. Seifert, M. W. Larsson, and L. R. Wallenberg: *Appl. Phys. Lett.* **85** (2004) 2077.
- 16) W. I. Park, D. H. Kim, S. W. Jung, and S. C. Yi: *Appl. Phys. Lett.* **80** (2002) 4232.
- 17) S. C. Liu and J. J. Wu: *J. Mater. Chem.* **10** (2002) 3125.
- 18) J. J. Wu and S. C. Liu: *Adv. Mater.* **14** (2002) 215.
- 19) M. H. Huang, Y. Wu, H. Feick, N. Tran, E. Weber, and P. Yang: *Adv. Mater.* **13** (2001) 113.
- 20) L. Vayssieres, K. Keis, S. E. Lindquist, and A. Hagfeldt: *J. Phys. Chem.* **105** (2001) 3350.
- 21) Z. R. Tian, J. A. Voigt, J. Liu, B. McKenzie, M. J. Mcdermott, M. A. Rodriguez, H. Konishi, and H. Xu: *Nat. Mater.* **2** (2003) 821.
- 22) Y. Li, G. S. Cheng, and L. D. Zhang: *J. Mater. Res.* **15** (2000) 2305.
- 23) Y. C. Wang, I. C. Leu, and M. H. Hon: *Electrochem. Solid State Lett.* **5** (2002) C53.
- 24) Y. C. Wang, I. C. Leu, and M. H. Hon: *J. Cryst. Growth* **237** (2002) 564.
- 25) M. J. Height, L. Mädler, and S. E. Pratsinis: *Chem. Mater.* **18** (2006) 572.
- 26) T. Q. Liu, O. Sakurai, N. Mizutani, and M. Kato: *J. Mater. Sci.* **21** (1986) 3698.
- 27) R. J. Lang: *J. Acoust. Soc. Am.* **34** (1962) 6.
- 28) H. Xu, X. Liu, D. Cui, M. Li, and M. Jiang: *Sens. Actuators B* **114** (2006) 301.
- 29) R. Tena-Zaera, A. Katty, S. Bastide, C. Lévy-Clément, B. O'Regan, and V. Munõz-Sanjósé: *Thin Solid Films* **483** (2005) 372.
- 30) C. Lévy-Clément, A. Katty, S. Bastide, F. Zenia, I. Mora, and V. Munõz-Sanjósé: *Physica E* **14** (2002) 229.
- 31) P. Hoyer and H. Weller: *J. Phys. Chem.* **99** (1995) 14096.
- 32) H. Rensmo, K. Keis, H. Lindstorm, S. Sodergren, A. Solbrand, A. Hagfeldt, and S. E. Lindquist: *J. Phys. Chem. B* **101** (1997) 2598.
- 33) R. S. Wagner and W. C. Ellis: *Appl. Phys. Lett.* **4** (1964) 89.
- 34) K. Hiruma, M. Yazawa, T. Katsuyama, K. Ogawa, K. Haraguchi, M. Koguchi, and H. Kakibayashi: *J. Appl. Phys.* **77** (1995) 447.
- 35) J. C. Viguié and J. Spitz: *J. Electrochem. Soc.* **122** (1975) 585.
- 36) V. Bilgin, S. Kose, F. Atay, and I. Akyuz: *J. Mater. Sci.* **40** (2005) 1909.
- 37) Z. V. Marinković, L. Mančić, and O. Milošević: *J. Eur. Ceram. Soc.* **24** (2004) 1929.
- 38) Y. Lee, H. Kim, and Y. Roh: *Jpn. J. Appl. Phys.* **40** (2001) 2423.
- 39) J. Hu and R. H. Gordon: *J. Appl. Phys.* **71** (1992) 880.
- 40) W. W. Wenas, A. Yamada, M. Konagai, and K. Takahashi: *Jpn. J. Appl. Phys.* **30** (1991) L441.
- 41) T. Q. Liu, O. S. N. Mizutani, and M. Ka: *J. Mater. Sci.* **21** (1986) 3698.
- 42) S. Major, A. Banerjee, and K. L. Chopra: *Thin Solid Films* **108** (1983) 333.
- 43) G. Blandenet, M. Court, and Y. Lagrade: *Thin Solid Films* **77** (1981) 81.
- 44) J. Aranovich and A. Oritz: *J. Vac. Sci. Technol.* **16** (1979) 994.